TITLE

The mitochondrial calcium uniporter regulates mitochondrial mass and dendritic localization in distinct hippocampal circuits

AUTHORS

Katy Pannoni[1], Daniela Gil[1], Logan Campbell[1], Shannon Farris[1-3,#]

AFFILIATIONS

[1]Fralin Biomedical Research Institute at Virginia Tech Carilion, Center for Neurobiology Research, Roanoke, Virginia

[2]Department of Biomedical Sciences & Pathobiology, Virginia-Maryland College of Veterinary Medicine, Virginia Tech, Blacksburg, Virginia

[3]Virginia Tech Carilion School of Medicine, Roanoke, Virginia

[#]Lead author, correspondence**:** farrissl@vtc.vt.edu

KEYWORDS

Mitochondrial calcium uniporter, Hippocampal CA2, Mitochondrial morphology, Mitochondrial localization, Dendrites, Entorhinal cortex

ABSTRACT

CA2 is an understudied subregion of the hippocampus that is critical for social memory. Previous studies identified multiple components of the mitochondrial calcium uniporter (MCU) complex as selectively enriched in CA2, however the functional significance of this enrichment remains unclear. The MCU complex regulates calcium entry into mitochondria, which in turn regulates mitochondrial transport and localization to active synapses. We found that MCU is strikingly enriched in CA2 distal apical dendrites, precisely where CA2 neurons receive entorhinal cortical input carrying social information. Further, MCU-enriched mitochondria in CA2 distal dendrites are larger compared to mitochondria in CA2 proximal apical dendrites and neighboring CA1 apical dendrites. Genetic knockdown of MCU in CA2 resulted in smaller mitochondria in CA2 distal dendrites, indicating that MCU expression plays a role in regulating mitochondrial mass in CA2. MCU overexpression in neighboring CA1 led to larger mitochondria preferentially in proximal dendrites compared to distal dendrites and GFP controls. Our findings demonstrate that mitochondria are molecularly and structurally diverse across hippocampal cell types and circuits, and that MCU expression cell-autonomously regulates mitochondrial mass, but layer-specific dendritic localization depends on cell type. Our data support the idea that CA2 mitochondria are functionally distinct from CA1 mitochondria, which may confer unique synaptic and circuit properties underlying CA2 function in social memory.

INTRODUCTION

Mitochondria are critical organelles that are responsible for a variety of functions in the cell, including generating energy, regulating calcium homeostasis, and signaling apoptosis (Duchen 2000; Vakifahmetoglu-Norberg, Ouchida, and Norberg 2017). There is mounting evidence of mitochondrial diversity across tissues and cell types (Sprenger and Langer 2019). In neurons, mitochondria are important for synaptic transmission, maintenance, and plasticity (Devine and Kittler 2018; Tang and Zucker 1997; Li et al. 2004; Stowers et al. 2002). Mitochondria are commonly found in axon terminals, as well as other sites with high energetic demand, and the loss of presynaptic mitochondria results in defective synaptic transmission (Stowers et al. 2002). Less is known about the role of mitochondria at the post-synapse. Li et al. demonstrated that the proper localization of mitochondria in cultured hippocampal neuron dendrites is also critical to support synapses. Specifically, increasing either mitochondrial content or mitochondrial activity in dendrites increased the number of spines and synapses (Li et al. 2004). In turn, synaptic activity can regulate the motility of mitochondria in dendrites, leading to an accumulation of mitochondria near recently active synapses (Li et al. 2004). Interestingly, the morphology and the distribution of mitochondria differs between axons and dendrites *in vivo* and *in vitro* (Chang, Honick, and Reynolds 2006, Lewis et al. 2018), and mitochondria in the two compartments are differentially modulated by synaptic activity in culture (Chang, Honick, and Reynolds 2006). Taken together, the morphology and localization of mitochondria can vary dynamically across different cellular compartments based on specific local needs. However, the functional consequence of this diversity remains elusive.

Previously, we transcriptionally profiled the major subregions of the mouse hippocampus (CA1, CA2, CA3 and Dentate Gyrus) and found that transcripts related to mitochondrial function are selectively enriched in CA2 (Farris et al. 2019), a region that is essential for social memory (Hitti and Siegelbaum 2014; Stevenson and Caldwell 2014; Dudek, Alexander, and Farris 2016). In particular, we found that multiple components of the mitochondrial calcium uniporter (MCU) complex are enriched in CA2, including the main pore forming subunit MCU, its calcium-sensing regulatory protein mitochondrial calcium uptake 1 (MICU1), and the MCU scaffolding protein mitochondrial calcium uniporter regulator 1 (MCUR1). The MCU complex is located on the inner mitochondrial membrane and regulates calcium entry into the mitochondria (Baughman et al. 2011; De Stefani et al. 2011). Although the exact role of MCU in regulating mitochondrial function is still being explored, it has been shown that calcium influx into the mitochondrial matrix stimulates ATP production via the TCA cycle (Wescott et al. 2019; Llorente-Folch et al. 2015), causes morphological changes by inducing fission and mitochondrial fragmentation (Han et al. 2008), and regulates the transport of mitochondria and the localization of mitochondria at active synapses (Wang and Schwarz 2009). However, whether cell-specific differences in MCU expression contribute to differences in mitochondrial morphology or localization is unknown.

Here, we look at the heterogeneity of MCU expression across the mouse hippocampus and test whether MCU expression plays a role in regulating the size and localization of mitochondria. We found that MCU was strikingly enriched in CA2 distal apical dendrites compared to proximal dendrites, an enrichment not seen in neighboring CA1 distal apical dendrites. MCU-enriched mitochondria in CA2 distal dendrites were more tubular in shape, significantly larger and fewer in number compared with proximal dendrites. CA2 distal dendrites receive distinct inputs compared to proximal dendrites, meaning that mitochondria display circuit-specific heterogeneity in CA2. Genetic knockdown of MCU in CA2 or overexpression of MCU in CA1 bidirectionally impacted mitochondrial mass, but the asymmetric distribution of MCU-labeled mitochondria in dendrites was cell-specific. These data shine light on the molecular and morphological diversity of mitochondria across hippocampal cell types and circuits, and suggest that mitochondria may be key regulators in shaping input-specific responses.

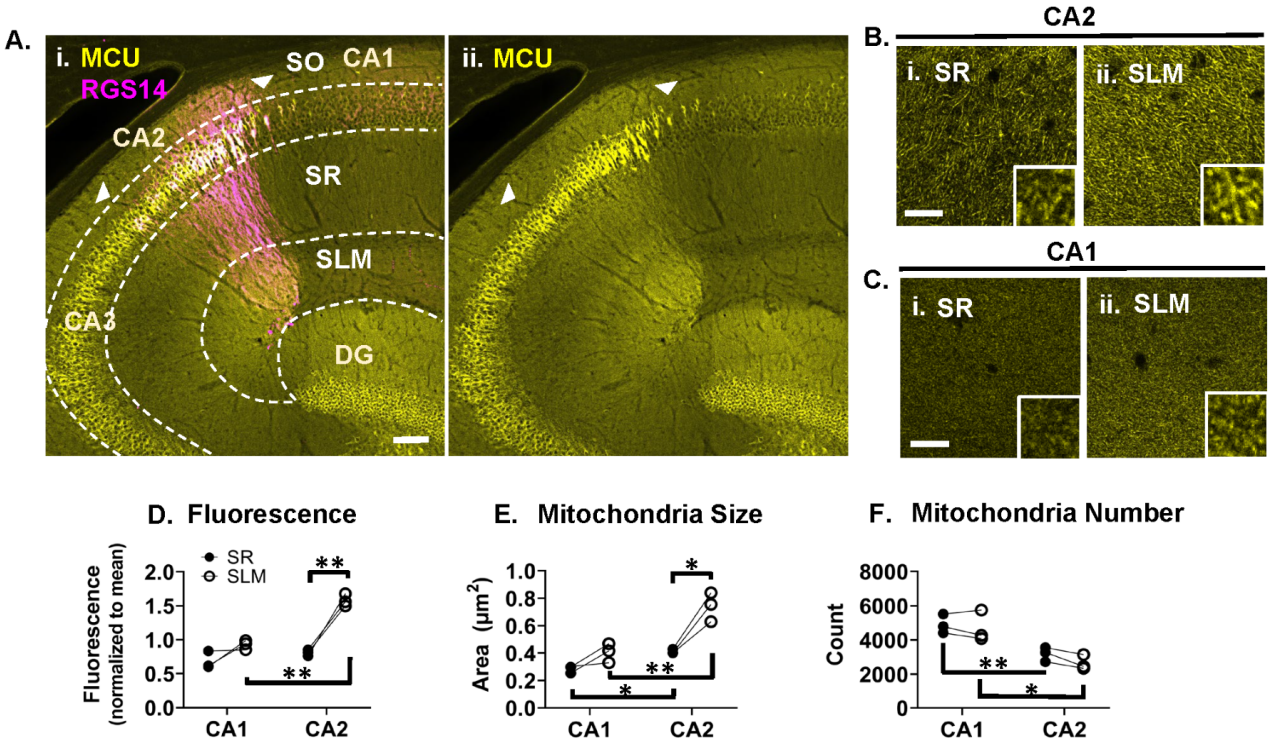

Figure 1: CA2 distal dendrites are preferentially enriched for MCU-labeled mitochondria

A. (*i.*) 20X epifluorescence tile image of a wild-type hippocampus stained for MCU (yellow) and RGS14 (magenta) with the subregions and dendritic layers labeled. White arrowheads indicate the borders of CA2. (*ii.*) The MCU channel alone.

B. Representative 40X confocal images of MCU staining in SR (*i.*) and SLM (*ii.*) of CA2 in a wild-type mouse. All representative 40X images are from a single Z section. Insets in **B** and **C** are a zoomed 10 X 10 µm crop of the larger image.

C. Representative 40X confocal images of MCU staining in SR (*i.*) and SLM (*ii.*) of CA1 in a wild-type mouse. Images were processed identically to the representative images in **B** for comparison between CA1 and CA2.

D-F. Quantification of MCU mean fluorescence (**D**), MCU-labeled mitochondrial size (**E**), and mitochondrial count (**F**) in SR and SLM of CA1 and CA2. A 100 X 100 µm region was analyzed from each dendritic layer. Fluorescence was normalized to the average per section before averaging per animal. SR (closed circles) and SLM (open circles) of the same animal are paired with lines. Paired two-tailed t-tests; N = 3 animals; 4-5 hippocampal sections / animal.

SO = Stratum Oriens; SR = Stratum Radiatum, SLM = Stratum Lacunosum Moleculare.
* = P < 0.05; ** = P < 0.01
Scale for A = 100 µm; B-C = 20 µm.

RESULTS

MCU-labeled mitochondria are preferentially enriched in CA2 distal dendrites

In order to assess the heterogeneity of MCU expression across hippocampal circuits, we immunostained hippocampal-containing sections from C57bl6/J mice for MCU. Consistent with our transcriptome study (Farris et al. 2019), MCU fluorescence was highly enriched in RGS14-positive CA2 cell bodies compared to neighboring CA1 cell bodies (Fig. 1A). However, within CA2, MCU fluorescence was strikingly enriched in the distal apical dendrites in layer stratum lacunosum moleculare (SLM) compared to the proximal dendrites in layer stratum radiatum (SR, Fig. 1B). MCU fluorescence was not detected in interneurons or non-neuronal cells present in SR or SLM layers. The same level of MCU enrichment in CA2 SLM was not seen in neighboring CA1 SLM (Fig. 1C-D, paired t-test; CA2 SR vs SLM: P = 0.0091; CA1 SR vs SLM: P = 0.1669). The distal dendrites of CA2 (SLM) receive layer-specific input from entorhinal cortex layer II, whereas the proximal dendrites (SR) receive input from CA3. These data suggest that there is mitochondrial diversity across hippocampal cell types and even within dendritic domains of the same cells that reflect distinct hippocampal circuits.

To quantify differences in mitochondrial morphology across the dendritic layers of CA1 and CA2, individual MCU-labeled mitochondria were segmented and quantified to obtain the average mitochondrial area and count for each dendritic layer (see methods). Supplemental Figure 1 includes the data for all three dendritic layers (stratum oriens (SO), SR, and SLM); However, we focused our analyses on layers SR and SLM, as less is known about CA2 basal dendrites and thus results would be hard to interpret. We found that the average MCU-labeled mitochondrial area was significantly greater in SLM compared to SR in CA2, but not significantly different between SLM and SR in CA1 (Fig. 1E, paired t-test; CA2 SR vs SLM: P = 0.0258; CA1 SR vs SLM: P = 0.1225). Across both dendritic layers, MCU-labeled mitochondrial area was significantly larger in CA2 than in CA1 (paired t-test; CA1 SR vs CA2 SR: P = 0.0125; CA1 SLM vs CA2 SLM; P = 0.0038). Interestingly, the number of mitochondria was not significantly different between the two dendritic layers of CA2 (CA2 SR: 3,189 ± 190; CA2 SLM: 2654 ± 117; paired t-test, P = 0.062). However, the number of mitochondria was significantly less in CA2 than in CA1 for both dendritic layers (CA1 SR: 4910 ± 281; CA1 SLM: 4707 ± 259; paired t-test, CA1 SR vs CA2 SR: P = 0.0056; CA1 SLM vs CA2 SLM: P = 0.0173). Thus, MCU-enriched mitochondria in CA2 dendrites appear to be generally larger in size but fewer in count compared to CA1 dendrites.

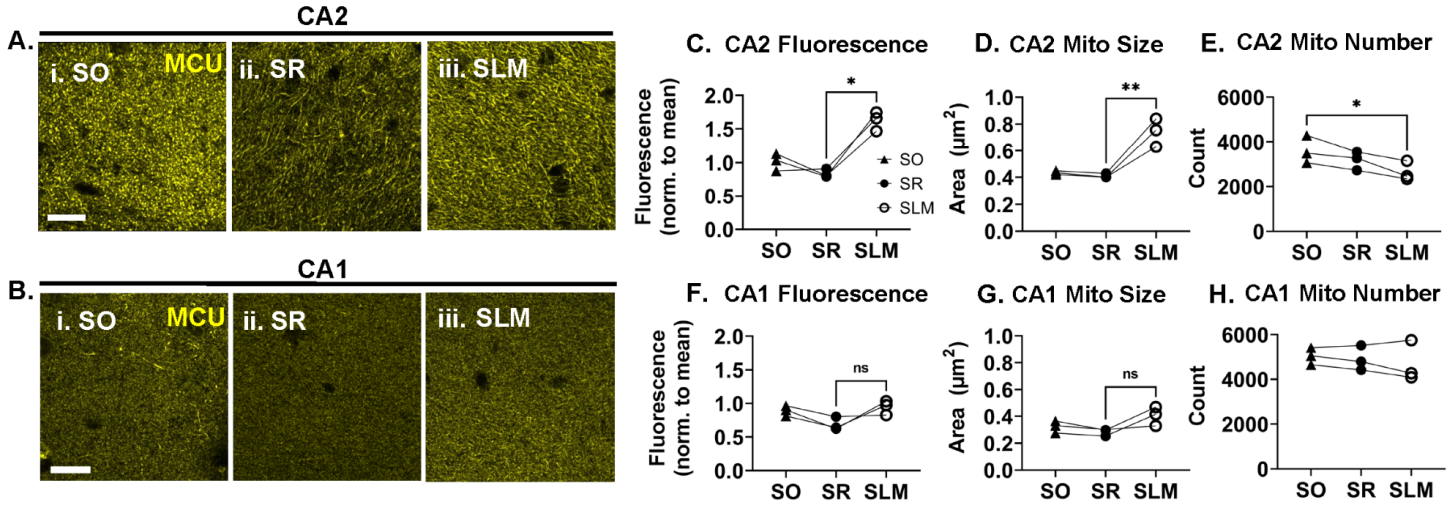

Supplemental Figure 1: CA2 distal synapses are preferentially enriched for MCU-labeled mitochondria

A. Representative 40X confocal images of MCU staining in SO (*i.*), SR (*ii.*) and SLM (*iii.*) of CA1 in the same wild-type mouse as in Figure 1B-C. Images of SR and SLM are the same images used in Figure 1.

B. Representative 40X confocal images of MCU staining in SO (*i.*), SR (*ii.*) and SLM (*iii.*) of CA2 in the same wild-type mouse.

C-E. Quantification of MCU mean fluorescence (**C**), MCU-labeled mitochondrial size (**D**), and mitochondrial count (**E**) in all three dendritic layers of CA2. A 100 X 100 µm region was analyzed from each dendritic layer and normalized the same as in Figure 1, with the addition of SO. Tukey's multiple comparison test; N = 3 animals; 4-5 hippocampal sections / animal. Overall effect of subregion was significant in CA2 with RM one-way ANOVA: Fluorescence: F = 26.8, P =0.0118 ; Size: F= 26.0 , P = 0.0011; Number: F = 23.5, P = 0.0077.

F-G. Quantification of MCU mean fluorescence (**F**), MCU-labeled mitochondrial size (**G**), and mitochondrial count (**H**) in all three dendritic layers of CA1 in the same hippocampal sections as **C-E**. Overall effect of subregion in CA1 was not significant with RM one-way ANOVA: Fluorescence: F = 4.6, P = 0.1550; Size: F = 5.4, P = 0.1325; Number: F = 0.94, P = 0.4339.

SO = Stratum Oriens; SR = Stratum Radiatum, SLM = Stratum Lacunosum Moleculare.
* = P < 0.05; ** = P < 0.01; ns = not significant.
Scale for A-B = 20 µm.

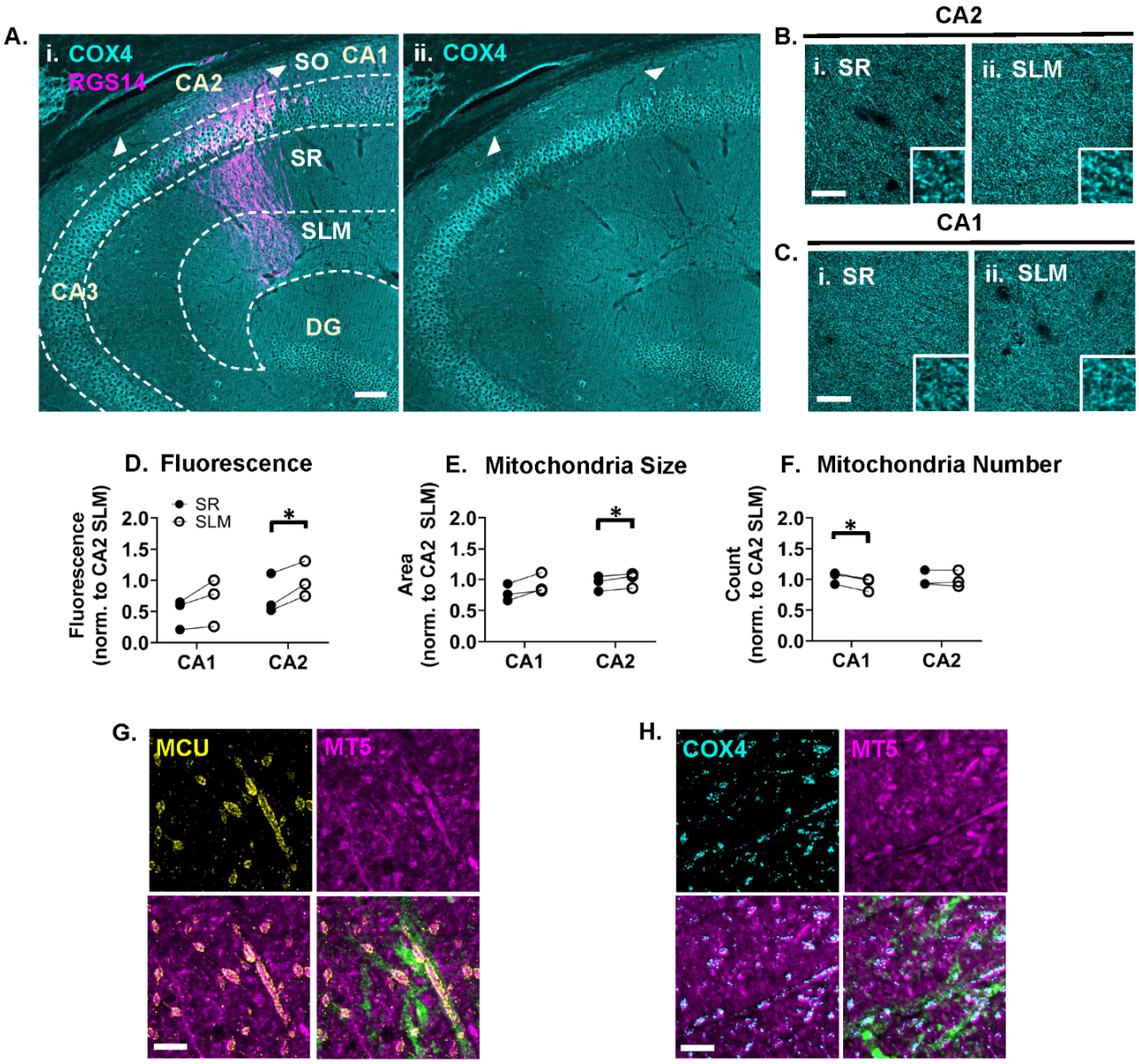

Figure 2: COX4 labels a broader but overlapping population of mitochondria than MCU.
A. (*i.*) 20X epifluorescence tile image of a wild-type hippocampus stained for COX4 (cyan) and RGS14 (magenta) with the subregions and dendritic layers labeled. White arrowheads indicate the borders of CA2. (*ii.*) The COX4 channel alone.
B. Representative 40X confocal images of COX4 staining in SR (*i.*) and SLM (*ii.*) of CA2 in a wild-type mouse. Insets in F and G are a zoomed 10 X 10 µm crop of the larger image.
C. Representative 40X confocal images of COX4 staining in SR (*i.*) and SLM (*ii.*) of CA1 in a wild-type mouse. Images in F and G were processed identically to preserve differences between subregions and dendritic layers.
D-F. Quantification of COX4 mean fluorescence (**D**), COX4-labeled mitochondrial size (**E**), and mitochondrial count (**F**) in SR and SLM of CA1 and CA2 normalized to the average of CA2 SLM. COX4 fluorescence was normalized to the average per section before normalization to CA2 SLM. Lines pair SR and SLM of the same animal together. Paired two-tailed t-tests; N = 3 animals.
G. Representative ProExM images of MCU (yellow) and MT-5 (magenta) in CA2 SLM. Bottom panels show the overlay of both channels (left) and an overlay with GFP+ CA2 distal dendrites (right).
H. Representative ProExM images of COX4 staining (yellow) and MT-5 staining (magenta) in CA2 SLM. An ROI was chosen which had a similar amount of MT-5 and GFP staining as in **G** for comparison.

* = $P < 0.05$; ** = $P < 0.01$
Scale for A = 100 µm; B-C = 20 µm; G-H = 3 µm (ExM adj.)

COX4 labels a broader but overlapping population of mitochondria than MCU

In addition to MCU, we stained for mitochondria using an antibody against cytochrome c oxidase subunit 4 isoform 1 (COX4), a component of the enzyme complex involved in the terminal step of the mitochondrial electron transport chain. Similar to MCU, COX4 staining was also enriched in CA2 cell bodies compared to neighboring CA1 cell bodies (Fig. 2A). In CA2 dendrites, we detected a small, but significant increase in COX4 fluorescence in SLM compared to SR (Fig. 2B,D; paired t-test, P = 0.0264) which was not significant between SR and SLM of CA1 (Fig. 2C; paired t-test, P = 0.1560). There was also a small, significant increase in COX4-labeled mitochondrial area between CA2 SR and SLM (Fig. 2E; paired t-test, P = 0.0422). Unlike with MCU-labeled mitochondria, there was no significant difference in the number of COX4-labeled mitochondria in CA1 versus CA2 for either dendritic layer (Fig. 2F; paired t-test, CA1 vs CA2 SR: P = 0.7178; CA1 vs CA2 SLM: P = 0.3547). In sum, COX4-labeled mitochondria show less of a layer specific preference or size difference between CA1 and CA2 compared to MCU-labeled mitochondria. To test the possibility that MCU is labeling a subpopulation of COX4-labeled mitochondria, we took super resolution images of MCU (Fig. 2G) and COX4 (Fig. 2H) labeled mitochondria in CA2 SLM alongside a novel pan-mitochondrial marker MT-5 (Kalyuzhny et al, 2021). We used protein retention expansion microscopy (ProExM) to visualize densely packed mitochondria (Campbell et al, 2021). In order to compare MCU and COX4 labeling across similar mitochondrial populations, we used ProExM images with similar MT-5 labeling and CA2 SLM dendrite labeling. Although MCU and COX4 similarly labeled the mitochondrial membrane surrounding MT-5 mitochondrial matrix labeling, MCU-labeled mitochondria were qualitatively larger and less numerous than COX4-labeled mitochondria. This suggests that MCU may label a subset of the mitochondrial population labeled with COX4.

CA2-specific MCU knockdown decreases mitochondrial size selectively in SLM

Next, we asked whether MCU expression plays a role in regulating the distinct mitochondrial morphology and localization to distal dendrites that we found in CA2. We generated CA2-specific MCU knockdown mice by crossing an Amigo2-cre line (Alexander et al. 2018) with an $MCU^{fl/fl}$ line (Luongo et al. 2015). The resulting heterozygous $MCU^{fl/wt}$; Amigo2-cre-positive mice ($MCU^{fl/wt}$ cre+) showed reduced MCU expression in CA2 neurons compared to control $MCU^{fl/wt}$; Amigo2-cre-negative mice ($MCU^{fl/wt}$ cre-) (Fig. 3A-C). We quantified the average size and number of MCU-labeled mitochondria of CA2 SR and SLM in $MCU^{fl/wt}$ cre+ and cre- mice as described for Figure 1. We found that MCU knockdown decreased the average size of MCU-labeled mitochondria in CA2 SLM compared to control cre- mice (Fig. 3D, Sidak's multiple comparison test: P = 0.0466), suggesting that MCU expression regulates mitochondrial size. Although mitochondrial size decreased, the number of MCU-labeled mitochondria was not significantly different in cre+ mice relative to cre- mice in either dendritic layer of CA2 (Fig. 3E, Sidak's multiple comparison test; SR: P = 0.5456; SLM: P = 0.0904). We next correlated mitochondrial area versus mitochondrial number comparing SR and SLM of cre+ (red diamonds) and cre- (blue circles) mice (Fig. 3F). We found that mitochondria in SLM (light shades) were more fragmented after MCU knockdown, both smaller and more numerous, while MCU knockdown had very little effect on mitochondria in SR (dark shades). However, as shown in the representative confocal images (Fig. 3AB), MCU-labeled mitochondria still appear to preferentially localize to SLM of CA2 in MCU knockdown mice. In both cre+ and cre- mice, MCU fluorescence and mitochondrial mass were greater in CA2 SLM compared to CA2 SR (paired t-test; cre+ SR vs SLM Fluorescence: P= <0.0001, Size: P= 0.0015; cre- SR vs SLM Fluorescence: P= <0.0001, Size: P= 0.0003), indicating that the localization of mitochondria to different dendritic compartments did not change with MCU knockdown.

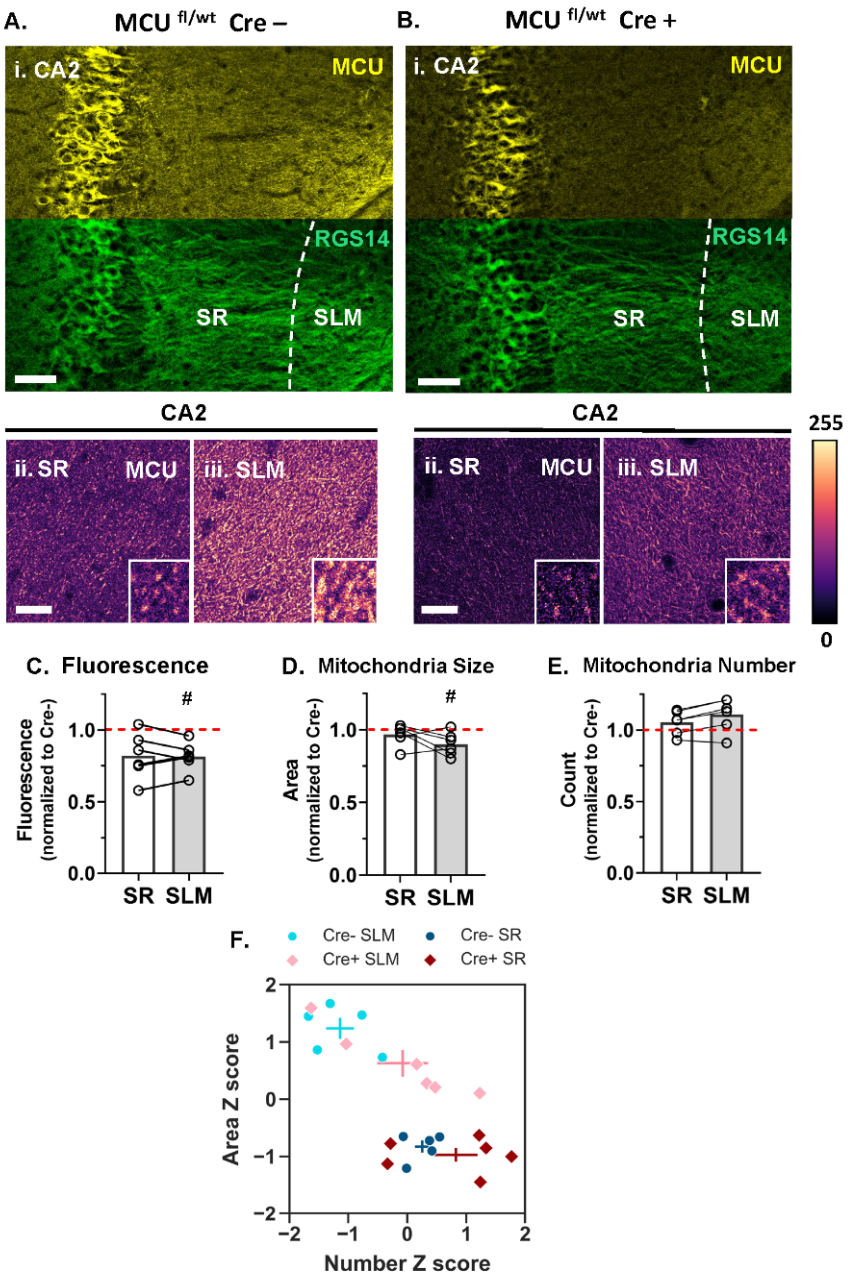

Figure 3: Knockdown of MCU in CA2 decreases mitochondrial size in the distal dendrites.

A. (i) Representative 20X epifluorescence image of CA2 stained for GFP (left) and MCU (right) in an MCU fl/wt cre- control mouse. Bottom: Representative 40X confocal images of MCU staining in SR (ii.) and SLM (iii.) of CA2 in of a different cre- control mouse. An intensity LUT has been applied to better visualize intensity differences. Inset shows a zoomed 10 x 10 µm crop.

B. (i) Representative 20X epifluorescence image of CA2 stained for GFP (left) and MCU (right) in an MCU fl/wt cre+ mouse. Images in A and B were processed the same to show the amount of MCU knockdown relative to control (A). Bottom: Representative 40X confocal images of MCU staining in SR (ii.) and SLM (iii.) of CA2 in a different cre+ mouse. The same LUT was applied as A.

C. Mean MCU fluorescence in SR and SLM of cre+ MCU fl/wt mice normalized to the control average (dashed red line). SR and SLM from the same animal are paired with lines. Data was normalized separately to the average of the cohort control. Sidak's multiple comparison test; N = 5-6 mice / group.

D. Average mitochondrial area in SR and SLM of the same MCU knockdown mice normalized to the control average (red line).

E. Mitochondrial number within a 100 X 100 µm ROI from SR and SLM of the same MCU knockdown mice in **C** and **D**. Data is normalized to the control average (red line).

F. Correlation plot of mitochondrial area versus mitochondrial number in SR (dark shades) and SLM (light shades) of Cre- (blue circles) and Cre+ animals (red diamonds). Average Z score is plotted for each animal with cross-hairs showing the mean and standard error of each group.

SR = Stratum Radiatum, SLM = Stratum Lacunosum Moleculare.
# = $P < 0.05$ comparing AAV-MCU to AAV-GFP within dendritic layer.
Scale for A-B(i.) = 50 µm; Scale for A-B(ii.-iii.) = 20 µm.

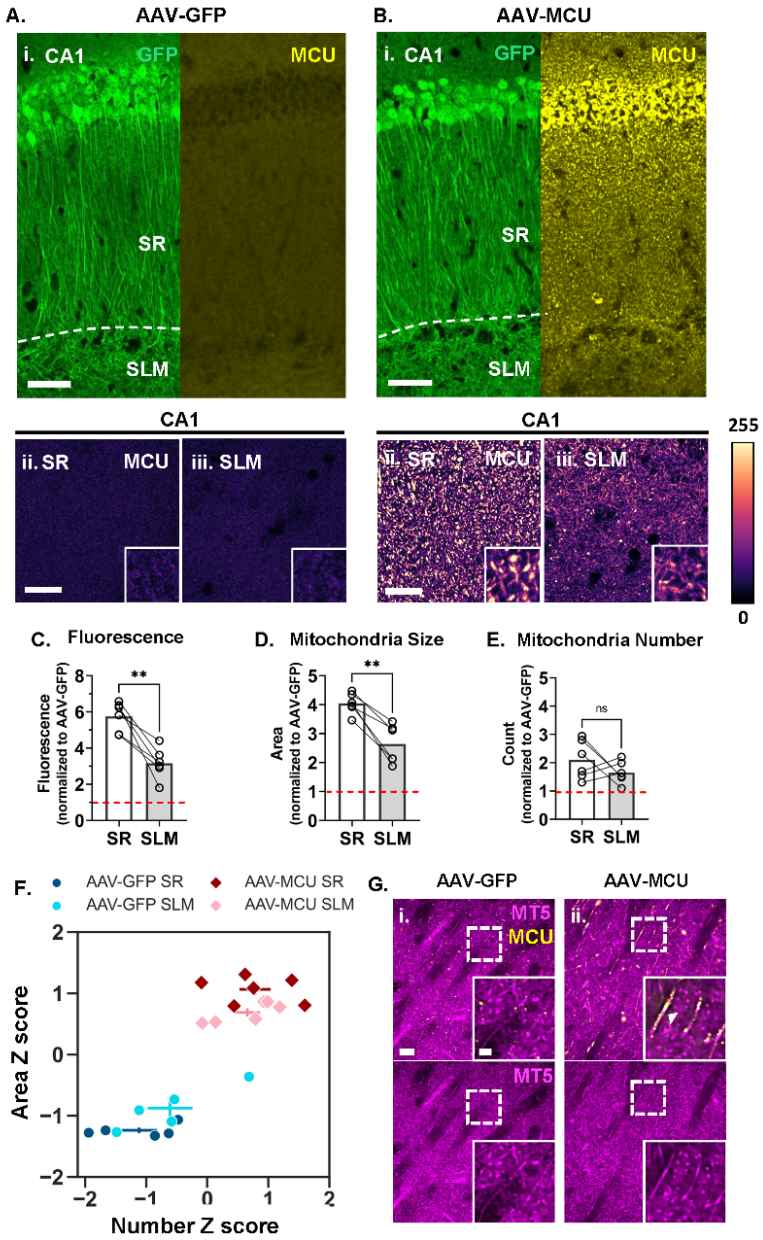

Figure 4: CA1 MCU overexpression increases mitochondrial size and influences layer-specific dendritic distribution

A. (i) Representative 20X epifluorescence image of CA1 stained for GFP (left) and MCU (right) in a AAV-GFP treated control animal. Bottom: Representative 40X confocal images of MCU staining in SR (i.) and SLM (ii.) of CA1 in a AAV-GFP treated mouse. Inset is a zoomed 10 X 10 µm crop.

B. (i) Representative 20X epifluorescence image of CA1 stained for GFP (left) and MCU (right) in an AAV-MCU treated mouse. Images in A and B were processed the same to maintain the relative difference between AAV-MCU and AAV-GFP control mice. Bottom: Representative 40X confocal images of MCU staining in SR (i.) and SLM (ii.) of CA1 in an AAV-MCU treated mouse.

C. Mean MCU fluorescence in SR and SLM of AAV-MCU mice normalized to the control average (red line). Lines connect SR and SLM of the same animal. N = 6 AAV-MCU mice and 5 AAV-GFP controls. AAV-MCU treatment significantly increased MCU fluorescence relative to AAV-GFP (two-way ANOVA, F = 190.9, P <0.0001).

D. MCU-labeled mitochondrial area in SR and SLM of the same AAV-MCU mice as in **C** normalized to the control average (red line). AAV-MCU treatment increased mitochondrial area relative to AAV-GFP (two-way ANOVA, F = 455.3, P <0.0001).

E. Mitochondrial number within a 100 X 100 µm ROI from SR and SLM of the same mice in C and D. Data is normalized to the control average (red line). AAV-MCU treatment increased mitochondrial number relative to AAV-GFP (two-way ANOVA, F = 35.97, P <0.0001).

F. Correlation plot of mitochondrial area versus mitochondrial number in SR (dark shades) and SLM (light shades) of AAV-GFP (blue circles) and AAV-MCU animals (red diamonds). Average Z score is plotted for each animal with cross-hairs showing the mean and standard error of each group.

G. Representative ProExM images of MT-5 (magenta) and MCU labeling (yellow) in CA1 SR of an AAV-GFP (i) and AAV-MCU (ii) mouse. Dashed box shows the location of the zoomed image in the inset. White arrow shows an example of a large MT-5 and MCU+ mitochondria. Bottom: Same images as above, but only the MT-5 channel.

SR = Stratum Radiatum, SLM = Stratum Lacunosum Moleculare.
* = P < 0.05; ** = P < 0.01; ns = not significant.
Scale for A-B(i.) = 50 µm; Scale for A-B(ii.-iii.) = 20 µm; Scale for G = 3 µm, inset = 1 µm (ExM adj.)

CA1 MCU overexpression increases mitochondrial size and influences layer-specific dendritic distribution

Based on our findings that knockdown of MCU expression in CA2 neurons decreases mitochondrial size in distal dendrites, we next asked whether increasing MCU expression can increase mitochondrial size in dendrites. To test this, we used adeno-associated viral vectors (AAVs) to overexpress MCU or GFP in CA1 neurons, which normally have 4-fold less MCU expression than CA2 neurons. CA1 was stereotaxically targeted in wild-type mice to infuse either MCU-2A-GFP (AAV-MCU, AAV9-hSYN-mMCU-2A-GFP-WPRE) or GFP (AAV-GFP, AAV9-hSYN1-eGFP) as a control. We then immunostained for MCU and GFP and quantified the mean MCU fluorescence and the size and number of MCU-labeled mitochondria in SR and SLM of CA1. MCU expression was about ~4.5-fold greater overall in the AAV-MCU treated mice than the control AAV-GFP treated mice (Fig. 4A-C). MCU overexpression in CA1 resulted in larger and more numerous MCU-labeled mitochondria across all dendritic layers of CA1 compared to GFP control mice (Fig. 4D-E). This confirms that MCU overexpression is sufficient to increase mitochondrial size in CA1. However, the effect of MCU overexpression on MCU fluorescence and mitochondrial size was greater in CA1 SR compared to SLM (Fig. 4C-D (Tukey's multiple comparison test; Fluorescence: $P = 0.0084$, Size: $P = 0.0033$). This indicates that, in contrast to CA2 dendrites where MCU expression preferentially impacts mitochondria in distal dendrites, MCU overexpression in CA1 preferentially influences mitochondrial size and localization in proximal dendrites compared with distal dendrites. As with CA2, proximal dendrites in CA1 receive layer specific input from area CA3, but in contrast to CA2, CA1 distal dendrites receive input from entorhinal cortex layer III. Again, suggesting that distinct hippocampal circuits are differentially regulated by diverse pools of mitochondria. In Fig. 4F, is the correlation between mitochondrial area versus mitochondrial number in AAV-MCU (red diamonds) and AAV-GFP (blue circles) treated mice. In AAV-MCU overexpression mice, CA1 SR was enriched with MCU-labeled mitochondria compared to SLM, as demonstrated by an increase in both mitochondrial size and number shifting the data towards the upper quadrant of the plot (Fig. 4F). This is in contrast to what we saw in AAV-GFP control mice, where mitochondria showed a slight preferential enrichment in SLM relative to SR. Mitochondria labeled with MT-5 also appear to be qualitatively larger and fewer in number in CA1 SR of AAV-MCU treated mice compared to AAV-GFP treated mice (Fig. 4G). In particular, long tubular MT-5 labeled mitochondria observed in AAV-MCU treated mice were generally colocalized with MCU (white arrow in Fig. 4G(ii.)).

DISCUSSION

The goal of this study was to investigate mitochondrial heterogeneity in the mouse hippocampus. Focusing on the enrichment of the MCU complex in area CA2, we unexpectedly uncovered that MCU expression is preferentially enriched in CA2 distal apical dendrites, precisely where CA2 neurons receive layer-specific input from entorhinal cortex II, a circuit recently proposed to carry social information to CA2 (Lopez-Rojas et al. 2021). We further found that MCU-enriched mitochondria in CA2 distal dendrites are larger and more tubular compared with mitochondria in CA2 proximal dendrites and CA1 apical dendrites. In line with what we found, it has been shown that genetically-labeled mitochondria in CA1 distal dendrites are more tubular than in proximal dendrites (Lee et al. 2019); However, our data suggest that the difference between mitochondria in the distal and proximal dendrites of CA2 is even more pronounced. Studies in cultured hippocampal neurons have demonstrated that elongated mitochondria in axons can take up more calcium, suggesting a direct connection between mitochondrial morphology and function (Lewis et al. 2018). In addition, we found molecular heterogeneity between CA2 and CA1 mitochondria in their expression of MCU relative to other mitochondrial markers such as COX4, with CA2 mitochondria showing a striking enrichment of MCU not seen in CA1. Given that COX4-labeled mitochondria appear to be more numerous than MCU across a comparative population of MT-5-labeled mitochondria, MCU may be labeling a subset, or specific microdomains of mitochondria that partially overlap with COX4-labeled mitochondria. These unique mitochondrial properties in CA2 suggest that layer-specific differences in mitochondrial function may contribute to the unique ability of CA2 neurons to encode social memory.

There are at least two possible reasons for why mitochondria are different in CA2 distal apical dendrites. Firstly, the dendritic layers receive layer-specific inputs which have different efficacies for generating somatic responses. Inputs that are more proximal to the soma typically cause a larger somatic excitatory postsynaptic current (EPSC); however, ECII inputs onto the distal dendrites of CA2 drive an unusually robust response in CA2 neurons, 5 to 6-fold larger EPSCs than those evoked from ECIII inputs onto CA1 neurons (Srinivas et al. 2017, but see also Sun et al. 2021). This enhanced efficacy is the result of unique synaptic and dendritic properties in CA2 SLM (Srinivas et al. 2017; Sun et al. 2014), including almost 3 times as many glutamatergic synapses in CA2 SLM than in CA1 SLM (Srinivas et al. 2017), although there is heterogeneity in CA2 dendritic SLM morphology (Helton et al 2019). Moreover, there is an asymmetrical gradient of innervation from ECII, with the lateral entorhinal cortex II (LECII) axons covering a larger area more distal from the soma than the medial entorhinal cortex II axons (MECII) (Steward, 1976). This is consistent with the asymmetric pattern of MCU-labeled mitochondrial morphology in CA2 dendrites. Notably, input from the LECII, but not the MECII, carries social information relevant to social recognition memory (Lopez-Rojas et al. 2021). CA2 SLM may have higher expression of MCU and greater mitochondrial mass than CA1 SLM in order to metabolically support more numerous and more active synapses. In the cerebellum, higher expression of MCU in granule cells compared to Purkinje cells and astrocytes correlated with greater mitochondrial calcium uptake and buffering capacity (Fecher et al. 2019), which is associated with an increase in ATP production (Wescott et al. 2019). Future studies will be needed to expand on whether there are layer specific differences in metabolic demand.

Secondly, the two separate circuits in CA2 also have distinct plasticity profiles. Synapses from CA3 onto CA2 SR are known to be resistant to long-term potentiation (LTP, Zhao et al. 2007; Simons et al. 2009), while synapses in CA2 SLM from the entorhinal cortex readily express LTP (Chevaleyre and Siegelbaum 2010). As a result, the more plastic synapses in CA2 SLM may have a higher metabolic demand than the less plastic synapses in CA2 SR. It is known that mitochondria are actively recruited to the presynapse, where it is thought that they locally regulate ATP and cytoplasmic calcium to support synaptic transmission (Chang, Honick, and Reynolds 2006). In axons, MICU3, a brain-specific regulator of MCU, is necessary for activity-dependent mitochondrial calcium uptake and ATP synthesis to fuel synaptic transmission (Ashrafi et al. 2020). At the post-synapse, repeated stimulation of cultured hippocampal neurons induces mitochondria to invade enlarged spines in an NMDA-dependent manner (Li et al. 2004), which in theory could support a plasticity-induced

increase in energetic demand. Studies have further shown that dendritic mitochondria in cultured neurons serve as a local energy source to fuel local translation-dependent changes at synapses during plasticity (Rangaraju et al. 2019). Similarly, the tubular, MCU-enriched mitochondria in the distal dendrites of CA2 could support the increased propensity for plasticity at these synapses. Given the role of MCU in calcium buffering and homeostasis, it is also possible that MCU plays a more direct role in LTP by regulating cytoplasmic calcium levels. We have previously shown that pharmacological blockade of mitochondrial calcium influx through MCU with Ru360 results in changes to the plasticity-resistant profile of CA2 SR synapses (Farris et al. 2019). However, it remains to be tested how MCU-enriched CA2 SLM synapses respond to MCU blockade. Other studies have shown that MCU overexpression can increase mitochondrial calcium uptake after NMDA receptor activation (Qiu et al. 2013). In addition, mitochondrial fission, which is regulated by calcium influx into mitochondria, is required for structural LTP in CA1 (Divakaruni et al. 2019). However, the exact role MCU might be playing in CA2 SLM is still an open question.

We next examined the role of MCU in regulating mitochondrial morphology and localization by knocking down MCU in CA2 neurons. In heterozygous $MCU^{fl/wt}$ cre+ knockdown mice, we observed a decrease in the size of MCU-labeled mitochondria in SLM of CA2 relative to cre- control mice. This demonstrates that MCU impacts mitochondrial size in CA2. However, the size effect observed was small and we saw considerable variability in the amount that these mice knocked down MCU, with some cre+ mice having similar MCU fluorescence as the control cre- mice (see Figure 2C(*i.*)). This could be due to compensation from the unaffected allele. Interestingly, we did not detect a difference in mitochondrial localization; MCU fluorescence and mitochondrial mass remained greater in CA2 SLM compared to CA2 SR of heterozygous MCU knockdown mice. Homozygous MCU knockout mice might induce a larger effect on mitochondrial size or localization, which may or may not be limited to SLM.

Lastly, we overexpressed MCU in CA1 and found that mitochondrial size was increased in MCU-labeled mitochondria and their dendritic distribution changed to preferentially localize to the proximal dendrites of CA1 compared to the control GFP mice. Contrary to our results, studies have shown that calcium influx into mitochondria leads to mitochondrial fission via phosphorylation of dynamin-related protein 1 (DRP1), resulting in more fragmented mitochondria (Zheng et al. 2017, Zhao et al, 2015, Kedra et al, 2021). However, the vast majority of these studies have been in disease models or in culture, and not much is known about the role of MCU in regulating mitochondrial mass in intact adult neuronal circuits as described in the present study. There is evidence that the balance of mitochondrial fission and fusion is regulated by activity in neurons (Li et al. 2004). Interestingly, age related changes in mitochondrial size have been reported in CA1 axons of adult mice compared to P15 mice in response to theta-burst stimulation (TBS), with TBS resulting in an increase in mitochondrial volume through fusion in adults (Smith et al, 2016). In addition, studies using isolated mitochondria have shown that increased oxidative phosphorylation stimulates mitochondrial fusion and elongation (Mishra et al. 2014), and it has been suggested that mitochondrial clusters can more efficiently distribute energy far distances (Amchenkova et al. 1988). Thus, it is possible that MCU overexpression increases oxidative phosphorylation, which in turn increases mitochondrial mass.

We also found that MCU overexpression caused a relatively greater increase in MCU-labeled mitochondrial size in SR compared to SLM of CA1, potentially because synapses in CA1 SR are more efficient at triggering action potentials, and therefore more metabolically demanding than synapses in CA1 SLM (Chevaleyre and Siegelbaum, 2010). These data demonstrate that MCU expression can regulate both size and mitochondrial localization in CA1, even though we did not detect a change in mitochondrial localization when we knocked down MCU in CA2. These differences suggest that the role of MCU in regulating mitochondrial localization in dendrites is dependent on the local calcium dynamics in each cell-type, presumably with MCU-enriched mitochondria driving localization to dendritic domains with greater calcium influx and/or metabolic demand. We previously showed that blocking MCU pharmacologically has a differential effect on baseline synaptic responses in CA1 and CA2 (Farris et al. 2019), indicating that mitochondrial calcium is regulated differently

286 between subregions. Other studies have shown that CA2 has a uniquely high capacity for calcium buffering
287 and calcium extrusion relative to the other CA regions (Simons et al. 2009). CA2 also has a lower ratio of
288 MICU1:MCU than CA1 (Farris et al. 2019), which has been associated with a lower threshold for mitochondrial
289 calcium uptake in cardiac and skeletal muscle tissue (Paillard et al. 2017). Differences in the local calcium
290 environment or the ratio of MCU complex components may explain the different results we see for CA1
291 compared to CA2. Alternatively, it is possible that the knockdown of MCU we achieved in the heterozygous
292 $MCU^{fl/wt}$ mice was insufficient to observe a change in mitochondrial localization or that other regulatory
293 components of the MCU complex were altered by MCU overexpression or knockdown and impacted cell-
294 specific results. Taken together, our results demonstrate that there is cell and circuit-specific diversity in
295 mitochondrial protein expression and morphology in the mouse hippocampus. This mitochondrial diversity
296 likely has functional consequences on cell and circuit function. We showed that MCU is a key regulator of, or
297 contributor to, mitochondrial diversity in dendrites, specifically with regards to mitochondrial mass and
298 asymmetric distribution. Local regulation of mitochondria could be an additional tool that neurons use to shape
299 circuit-specific functions that drive behavior.

300 **METHODS**

301

302 **Animals**

303 The analysis of wild type MCU- and COX4-labeled mitochondria was done on adult Amigo2-EGFP reporter
304 mice (RRID:MMRRC 033018-UCD) of both sexes, which were bred for at least 10 generations onto a
305 C57BL/6J background. To generate CA2-specific MCU knockdown mice, Amigo2-cre mice (Alexander et al.,
306 2018) were crossed with homozygous MCU floxed mice (B6;129S-Mcutm1.1Jmol/J; Jax #: 029817) (Kwong et
307 al. 2015). Heterozygous $MCU^{fl/wt}$;Amigo2-cre +/-mice were used for the experiments in Figure 3. Ai14
308 TdTomato reporter mice on a C57BL/6J background (Jax #: 007914; Madisen et al. 2010) were used (in the
309 absence of cre) for the AAV infusion experiments in Figure 4. Mice were group-housed under a 12:12 light/dark
310 cycle with access to food and water ad libitum. All procedures were approved by the Animal Care and Use
311 Committee of Virginia Tech.

312

313 **AAV stereotaxic infusions**

314 Prior to surgery, mice received a subcutaneous injection of SR Buprenorphine (1.0mg/kg) for preemptive
315 analgesia and an intraperitoneal injection of ketamine/dexdomitor cocktail (ket 100mg/kg; dex 0.5mg/kg) for
316 anesthesia. Mice were put on an absorbent pad and eyes covered with ophthalmic lubricant before being
317 positioned into a stereotaxic apparatus with ear bars. The hair around the incision site was trimmed with
318 electric clippers, and the incision area cleaned with 3 cycles of alternating betadine and 70% alcohol. After
319 clearing the skull, a drill was used to make a unilateral burr hole targeting CA1 of the hippocampus (-2.1 AP; -
320 1.4 ML; -1.4DV). Using a glass pipette attached to a syringe pump, 0.1-0.3µl of AAV-MCU (AAV9-hSYN-
321 mMCU-2A-GFP-WPRE, Vector Biolabs, AAV-254662) or AAV-GFP (AAV9-hSYN1-eGFP, Vector Biolabs,
322 VB1107) was infused into the hippocampus at a flow rate of 100 nl/min. After five minutes, the glass pipette
323 was slowly retracted at a rate of 0.5 mm/min and the incision was closed with surgical glue. Mice were given
324 antisedan (atipamezole, 1mg/kg) and allowed to recover on a heating pad until ambulatory. Two weeks after
325 infusion, mice were given an overdose of sodium pentobarbital (150 mg/kg) and transcardially perfused with
326 4% paraformaldehyde then processed for immunohistochemistry as described below.

327 Due to the potential for MCU overexpression to cause cell death (Granatiero et al. 2019), we immunostained
328 AAV treated sections for MAP2 and GFAP. We found no evidence of cell death or gliosis in CA1 of the AAV-
329 MCU or AAV-GFP infused mice as was seen in mouse cortical neurons, but not zebrafish retina cone
330 photoreceptors (Hutto et al. 2020). We presume this is an indication that different cell types have various
331 capacities for MCU expression and/or mitochondrial calcium influx based intrinsic or extrinsic factors related to
332 calcium signaling.

333 **Immunofluorescence**
334 Mice were anesthetized with 150 mg/kg sodium pentobarbital and transcardially perfused with 15 ml of ice-cold
335 4% paraformaldehyde. Brains were dissected and post-fixed for at least 24 hours before sectioning 40 µm
336 thick sections in the horizontal plane on a vibratome (Leica VT1000S). All brain sections immunostained with
337 MCU or COX4 underwent antigen retrieval by boiling free floating sections for 3 min in 1ml of nanopure water,
338 followed by a permeabilization step in 0.03% Triton-100x for 15 min at room temperature. All sections were
339 then washed in PBS and blocked for 30-60 minutes in 5% Normal Goat Serum (NGS)/0.03% Triton-100x.
340 Sections were incubated overnight (18-24 hours) with primary antibodies, either rabbit-anti-MCU (1:500, Novus
341 NBPS-76948) or rabbit-anti-COX4 (1:500, SySy 298 003) with the addition of a chicken-anti-GFP antibody
342 (1:500, Abcam ab13970) or a chicken-anti-RFP antibody (1:500, SySy 409-006) for any tissue containing the
343 respective reporter. In some cases where CA2 was not labeled genetically, a mouse-anti-RGS14 antibody
344 (1:500, NeuroMab 75-170) was used to label CA2. After several rinses in PBS-T (0.03% Triton-100x), sections
345 were given a quick second block (10-20 minutes) before incubating in secondary antibodies for 2 hours at
346 room temperature. Secondary antibodies (1:500, Invitrogen, goat anti mouse-488, A11029; or goat anti rabbit-
347 546, A11034) were diluted in blocking solution. Prior to imaging, sections were washed in PBS-T and mounted
348 under Vectashield (Vector Laboratories) or Prolong gold fluorescence media with 4′,6-diamidino-2-phenylindole
349 (DAPI) (Invitrogen, P36931).
350
351 **Image acquisition and processing**
352 Images were acquired on an inverted Zeiss 700 confocal microscope equipped with a motorized stage,
353 405/488/561 laser lines, and a 40X/1.3NA lens; or on an inverted Leica Thunder imaging system with individual
354 LED lines, and 20X/0.8NA or 63 X/1.4NA lenses. Confocal images were acquired at 8-bit. All thunder images
355 were acquired at 16-bit, subjected to computational clearing, and then set to the same fluorescence range (eg.
356 0-1000) within analysis cohorts before converting to 8-bit in Fiji. All images within analysis cohorts were
357 acquired and processed identically to maintain relative differences in fluorescence.
358
359 **Quantification of ROI fluorescence and mitochondrial size and number**
360 The mean fluorescence, average size and number of MCU- or COX4-labeled mitochondria were quantified
361 using the image-analysis software Fiji (v. 2.1.0/1.53c, NIH) (Schindelin et al., 2012). When feasible, all
362 analyses were done blind to genotype or condition. A representative 100 x 100 µm ROI was selected in SO,
363 SR and SLM of each hippocampal section analyzed. For consistency, the brightest optical Z-slice that was in
364 focus was chosen for each ROI. Cell bodies, blood vessels and tears in the tissue were avoided as much as
365 possible when picking an ROI. A few of the ROIs were selected at an angle (by rotating the rectangular
366 selection tool) to avoid the tissue edge or any of the above-mentioned features.

367 Fiji's *measure* tool was used to get the mean fluorescence ("mean grey value") of the cropped ROI images.
368 Fluorescence was measured from the cropped 8-bit images with no other adjustments made. To get the
369 average mitochondrial size and number, individual mitochondria were segmented using "Nucleus Counter"
370 from Fiji's Cookbook Microscopy analysis plug-in. For the segmentation, we used an automated Otsu intensity
371 threshold and a size threshold of 5 – 500 pixels with median 3x3 smoothing. A general "noise" threshold below
372 which very few, if any, mitochondria were identified in the negative control images (without primary antibody)
373 was used when necessary to adjust the automated Otsu threshold. Once the mitochondria were properly
374 segmented, their areas were measured with the *measure* tool and exported in a .CSV file for further analysis
375 and plotting in Python and Prism.

376 **Analysis of mitochondria in wild-type CA1 and CA2**
377 40X confocal images of MCU-labeled mitochondria were segmented and quantified (as described above) from
378 CA1 and CA2 of 3 wild-type mice, 4 hippocampal sections per mouse. 63X Thunder images of COX4-labeled
379 mitochondria from CA1 and CA2 were similarly segmented and quantified in 3 different wild-type mice, 1
380 hippocampal section per mouse. Because MCU and COX4 were imaged at different scales on different
381 imaging systems, mitochondrial sizes can't be directly compared between the MCU and COX4 populations.

Background fluorescence was measured by measuring the mean fluorescence of a similar ROI from negative control images (without primary antibody) of each layer in both CA1 and CA2. The background fluorescence was subtracted from the mean fluorescence of each ROI, and then fluorescence was normalized to the section average (including SR and SLM of both CA1 and CA2) to account for section to section variability in staining. The same analysis was done for the COX4 images, except that the COX4 data was then normalized to the average of CA2 SLM for all three metrics. For plotting, the sections were averaged together to get animal averages and SR and SLM of the same animal are paired with lines. Paired two-tailed t-tests (uncorrected) were run comparing SR and SLM of each subregion and also comparing SR or SLM across CA1 and CA2. One-way ANOVAs with corrected posthoc tests were performed when SO, SR, SLM were compared as in Supplemental Fig 1.

Analysis of mitochondria after MCU knockdown in CA2

Similar to the analysis of MCU-labeled mitochondria in the wild-type hippocampus, MCU-labeled mitochondria were quantified in SR and SLM of CA2 in heterozygous $MCU^{fl/wt}$ X Amigo2-cre + or - mice. Mitochondria were quantified using 63X thunder images as described above. We analyzed 5 cre- and 6 cre+ mice across 3 separate rounds of staining with cre- and cre+ mice included in each run. Before quantifying, the fluorescence range was scaled separately and optimized for each IHC cohort to be visually similar across all cohorts before the images were converted to 8bit. Mitochondria were segmented with the same Otsu thresholding and size threshold as the wild-type images.

Results of the MCU knockdown were analyzed in Python with a custom code and then imported into Prism for final plotting and statistics. For this dataset, background fluorescence was not subtracted. The data for each metric (fluorescence, size and number) was normalized to the average cre– cohort control for each dendritic layer, and the normalized cre+ animal averages were plotted for SR and SLM (Fig. 2C). To compare dendritic layers across cre+ and - animals, the data were normalized to the cohort average to combine the cohorts and a two-way ANOVA was performed with a Sidak's multiple comparisons post hoc test.

Analysis of mitochondria after MCU overexpression in CA1

MCU-labeled mitochondria were quantified in SR and SLM of CA1 in 6 AAV-MCU and 5 AAV-GFP control mice. A 100 X 100 μm ROI was chosen from 63X Thunder images from each dendritic layer. MCU fluorescence, mitochondrial size and mitochondrial number were measured for each ROI as described above.

The AAV-MCU data was normalized to the average AAV-GFP cohort control for each layer. To test for an effect of MCU overexpression on mitochondria in each dendritic layer, multiple t-tests were run on the combined data comparing AAV-MCU to AAV-GFP mice within each layer, with Bonferroni correction for multiple comparisons. Then, to determine if the effect of MCU overexpression was significantly different between dendritic layers, a RM one-way ANOVA was performed on the combined MCU-AAV data that was normalized to the control, followed by Tukey's post-hoc test.

Protein-retention Expansion Microscopy (ProExM)

40μm horizontal mouse brain sections were expanded with 4X protein expansion microscopy (ProExM) as previously described in Campbell et al, 2021. All solutions were prepared as described by Asano et al, 2018. Sections to be expanded were incubated overnight in Acryloyl-X stock/PBS (1:100, ThermoFisher, A20770) at room temperature in the dark. Following incubation, the slices were washed twice with PBS for 15 minutes each at room temperature. The gelation solution was prepared by adding 384 uL of monomer solution, 8 uL 4-Hydroxy-TEMPO inhibitor (1:200 w/v, Sigma Aldrich, 176141), 8uL TEMED accelerator (10% v/v, Sigma Aldrich, T7024), and lastly 8uL of APS initiator (10% w/v, Sigma Aldrich, 248614) for each section. Sections were incubated in the gelation solution for 30 minutes at 4C in the dark. Gelated sections were placed on gelation chambers constructed from microscope slides with coverslips as spacers. Our gelation chambers produce gels with the thickness of a single No. 1.5 coverslip (~0.15mm thick). The chambers were filled with gelation solution and allowed to incubate at 37C for 2 hours in a humidified container. Following gelation, the gelation chamber was deconstructed and the gel was carefully removed from the chamber using a coverslip and Proteinase K-free digestion solution. Gels were then placed in digestion solution containing proteinase K (8U/mL, New England BioLabs, P8107S) and digested for 4 hours at room temperature. For the AAV

experiments, gels were placed in an alkaline buffer (100 mM Tris base, 5% (w/v) Triton X-100, 1% SDS) and digested with heat using an autoclave on the liquid cycle for 1 h at 121 C, which is a milder alternative to enzymatic digestion with Proteinase K, prior to antibody staining (Campbell et al. 2021, Asano et al. 2018). Proteinase K digested gels were immunostained prior to digestion instead. Gels were stained with DAPI (Sigma Aldrich, D9542; 1:10,000 in PBS) and MT-5 (gifted by Alex Kalyuzhny at Bio-Techne; 1:20,000 in PBS) for 30 minutes at room temperature with shaking. Kalyuzhny et al developed MT-5 as a novel mitochondrial marker specifically for use in fixed tissue (Kalyuzhny et al, 2021). MT-5 is a far-red fluorescence probe (655 nm excitation/669 nm emission) that localizes in mitochondria without cross-reacting with the cell nucleus or plasma membrane, and is highly photostable. Finally, the gels were washed twice with PBS for at least 20 minutes and either stored in PBS at 4C or fully expanded in npH20 for imaging. Images of CA2 SLM dendrites were acquired with 4X Super Resolution by Optical Pixel Reassignment (SoRa) using identical acquisition parameters on an inverted spinning disk confocal microscope (Yokogawa CSU-W1 SoRa/ Nikon Ti2-E Microscope) equipped with Hamamatsu Fusion BT cameras and a 20X water immersion lens (0.95 NA, WD 1.0 mm). Resulting images underwent native deconvolution and denoising using NIS-Elements Software.

Statistical analyses

A custom Python code was written to parse the segmented data from Fiji, get the average size and number of mitochondria for each ROI, and combine the segmented data with the ROI fluorescence of each ROI. Statistical analyses were done in python (v3.7.9) or Prism (Graphpad Prism 9) with an alpha of 0.05 considered significant.

DECLARATIONS

Funding

Research reported in this publication was supported by the National Institute of Mental Health of the NIH under award R00MH109626 and R01MH124997 to S.F. and by startup funds provided by Virginia Tech.
The funders had no role in the design of the study and collection, analysis, and interpretation of data and in writing the manuscript.

Authors' contributions

Conceptualization, S.F.; Methodology, K.E.P., D.G., L.A.C., S.F.; Formal Analysis, K.E.P., D.G., L.A.C., S.F.; Investigation, K.E.P., D.G., L.A.C., S.F.; Writing – Original Draft, K.E.P., S.F.; Writing – Review & Editing, K.E.P., D.G., S.F.; Visualization, K.E.P., D.G., L.A.C., S.F.; Supervision, S.F.; Funding Acquisition, S.F.

Acknowledgements

We thank the members of the Farris lab for providing feedback and critically reading this manuscript, as well as the Virginia Tech animal care staff for their support.

Conflict of interest

The authors declare that they have no competing interests.

FIGURE LEGENDS

Figure 1: CA2 distal synapses are preferentially enriched for MCU-labeled mitochondria

A. (*i.*) 20X epifluorescence tile image of a wild-type hippocampus stained for MCU (yellow) and RGS14 (magenta) with the subregions and dendritic layers labeled. White arrowheads indicate the borders of CA2. (*ii.*) The MCU channel alone.

B. Representative 40X confocal images of MCU staining in SR (*i.*) and SLM (*ii.*) of CA2 in a wild-type mouse. All representative 40X images are from a single Z section. Insets in **B** and **C** are a zoomed 10 X 10 µm crop of the larger image.

C. Representative 40X confocal images of MCU staining in SR (*i.*) and SLM (*ii.*) of CA1 in a wild-type mouse. Images were processed identically to the representative images in **B** for comparison between CA1 and CA2.
D-F. Quantification of MCU mean fluorescence (**D**), MCU-labeled mitochondrial size (**E**), and mitochondrial count (**F**) in SR and SLM of CA1 and CA2. A 100 X 100 µm region was analyzed from each dendritic layer. Fluorescence was normalized to the average per section before averaging per animal. SR (closed circles) and SLM (open circles) of the same animal are paired with lines. Paired two-tailed t-tests; N = 3 animals; 4-5 hippocampal sections / animal.

SO = Stratum Oriens; SR = Stratum Radiatum, SLM = Stratum Lacunosum Moleculare.
* = P < 0.05; ** = P < 0.01
Scale for A = 100 µm; B-C = 20 µm.

Figure 2: COX4 labels a broader but overlapping population of mitochondria than MCU
A. (*i.*) 20X epifluorescence tile image of a wild-type hippocampus stained for COX4 (cyan) and RGS14 (magenta) with the subregions and dendritic layers labeled. White arrowheads indicate the borders of CA2. (*ii.*) The COX4 channel alone.
B. Representative 40X confocal images of COX4 staining in SR (*i.*) and SLM (*ii.*) of CA2 in a wild-type mouse. Insets in F and G are a zoomed 10 X 10 µm crop of the larger image.
C. Representative 40X confocal images of COX4 staining in SR (*i.*) and SLM (*ii.*) of CA1 in a wild-type mouse. Images in F and G were processed identically to preserve differences between subregions and dendritic layers.
D-F. Quantification of COX4 mean fluorescence (**D**), COX4-labeled mitochondrial size (**E**), and mitochondrial count (**F**) in SR and SLM of CA1 and CA2 normalized to the average of CA2 SLM. COX4 fluorescence was normalized to the average per section before normalization to CA2 SLM. Lines pair SR and SLM of the same animal together. Paired two-tailed t-tests; N = 3 animals.
G. Representative Pro-ExM images of MCU (yellow) and MT-5 (magenta) in CA2 SLM. Bottom panels show the overlay of both channels (left) and an overlay with GFP+ CA2 distal dendrites (right).
H. Representative Pro-ExM images of COX4 staining (yellow) and MT-5 staining (magenta) in CA2 SLM. An ROI was chosen which had a similar amount of MT-5 and GFP staining as in **G** for comparison.

* = P < 0.05; ** = P < 0.01
Scale for A = 100 µm; B-C = 20 µm; G-H = 3 µm (ExM adj.)

Figure 3: Knockdown of MCU in CA2 decreases mitochondrial size in the distal dendrites.
A. (i) Representative 20X epifluorescence image of CA2 stained for GFP (left) and MCU (right) in an MCU fl/wt cre- control mouse. SR = Stratum Radiatum, SLM = Stratum Lacunosum Moleculare. Bottom: Representative 40X confocal images of MCU staining in SR (ii.) and SLM (iii.) of CA2 in of a different cre- control mouse. An intensity LUT has been applied to better visualize intensity differences. Inset shows a zoomed 10 x 10 µm crop.
B. (i) Representative 20X Thunder image of CA2 stained for GFP (left) and MCU (right) in an MCU fl/wt cre+ mouse. Images in A and B were processed the same to show the amount of MCU knockdown relative to control (A). Bottom: Representative 40X confocal images of MCU staining in SR (ii.) and SLM (iii.) of CA2 in a different cre+ mouse. The same LUT was applied as in A.
C. Mean MCU fluorescence in SR and SLM of cre+ MCU fl-wt mice normalized to the control average (red line). SR and SLM from the same animal are paired with lines. Data was normalized separately to the average of the cohort control. Sidak's multiple comparison test. N = 5-6 mice / group.
D. Average mitochondrial size in SR and SLM of the same MCU knockdown mice as in C. normalized to the control average (red line).
E. Mitochondrial number within a 100 X 100 µm ROI from SR and SLM of the same MCU knockdown mice in C and D. Data is normalized to the control average (red line).

F. Correlation plot of mitochondrial area versus mitochondrial number in SR (dark shades) and SLM (light shades) of Cre- (blue circles) and Cre+ animals (red diamonds). Average Z score is plotted for each animal with cross-hairs showing the mean and standard error of each group.

= P < 0.05 comparing MCU-AAV to GFP-AAV within dendritic layer.
Scale bar for A-B(i.): 50um; Scale bar for A-B(ii.-iii.): 20um.

Figure 4: CA1 MCU overexpression increases mitochondrial size and influences layer-specific dendritic distribution

A. (i) Representative 20X epifluorescence image of CA1 stained for GFP (left) and MCU (right) in a GFP-AAV treated control animal. SR = Stratum Radiatum, SLM = Stratum Lacunosum Moleculare. Bottom: Representative 40X confocal images of MCU staining in SR (i.) and SLM (ii.) of CA1 in a GFP-AAV treated mouse. Inset shows a zoomed 10 X 10 μm crop.

B. (i) Representative 20X epifluorescence image of CA1 stained for GFP (left) and MCU (right) in an MCU-AAV treated mouse. Images in A and B were processed the same to maintain the relative difference between MCU-AAV and GFP-AAV control mice. Bottom: Representative 40X confocal images of MCU staining in SR (i.) and SLM (ii.) of CA1 in an MCU-AAV treated mouse.

C. Mean MCU fluorescence in SR and SLM of MCU-AAV mice normalized to the control average (dashed red line). Lines connect SR and SLM of the same animal. N = 6 MCU-AAV mice and 5 GFP-AAV controls. MCU-AAV treatment significantly increased MCU fluorescence in MCU-AAV relative to GFP-AAV (two-way ANOVA, F = 190.9, P <0.0001).

D. MCU-labeled mitochondrial size in SR and SLM of the same MCU-AAV mice as in C. normalized to the control average (red dashed line). MCU-AAV treatment increased mitochondrial area relative to GFP-AAV (two-way ANOVA, F = 455.3, P <0.0001).

E. Mitochondrial number within a 100 X 100 μm ROI from SR and SLM of the same mice in C and D. Data is normalized to the control average (red line). MCU-AAV treatment increased mitochondrial number relative to GFP-AAV (two-way ANOVA, F = 35.97, P <0.0001).

F. Correlation plot of mitochondrial area versus mitochondrial number in SR (dark shades) and SLM (light shades) of AAV-GFP (blue circles) and AAV-MCU animals (red diamonds). Average Z score is plotted for each animal with cross-hairs showing the mean and standard error of each group.

G. Representative ProExM images of MT-5 (magenta) and MCU labeling (yellow) in CA1 of an AAV-GFP (i) and AAV-MCU (ii) mouse. Dashed box shows the location of the zoomed image in the inset. White arrow shows an example of a large MT-5 and MCU+ mitochondria. Bottom: Same images as above, but only the MT-5 channel.

* = P < 0.05; ** = P < 0.01; ns = not significant.
Scale bar for A-B(i.): 50um; Scale bar for A-B(ii.-iii.): 20um.

Supplemental Figure 1: CA2 distal synapses are preferentially enriched for MCU-labeled mitochondria

A. Representative 40X confocal images of MCU staining in SO (*i.*), SR (*ii.*) and SLM (*iii.*) of CA1 in the same wild-type mouse as in Figure 1B-C. Images of SR and SLM are the same images used in Figure 1.

B. Representative 40X confocal images of MCU staining in SO (*i.*), SR (*ii.*) and SLM (*iii.*) of CA2 in the same wild-type mouse.

C-E. Quantification of MCU mean fluorescence (**C**), MCU-labeled mitochondrial size (**D**), and mitochondrial count (**E**) in all three dendritic layers of CA2. A 100 X 100 μm region was analyzed from each dendritic layer and normalized the same as in Figure 1, with the addition of SO. Tukey's multiple comparison test; N = 3 animals; 4-5 hippocampal sections / animal. Overall effect of subregion was significant in CA2 with RM one-way ANOVA: Fluorescence: F = 26.8, P =0.0118; Size: F= 26.0, P = 0.0011; Number: F = 23.5, P = 0.0077.

F-G. Quantification of MCU mean fluorescence (**F**), MCU-labeled mitochondrial size (**G**), and mitochondrial count (**H**) in all three dendritic layers of CA1 in the same hippocampal sections as **C-E**. Overall effect of subregion in CA1 was not significant with RM one-way ANOVA: Fluorescence: F = 4.6, P = 0.1550; Size: F = 5.4, P = 0.1325; Number: F = 0.94, P = 0.4339.

581 SO = Stratum Oriens; SR = Stratum Radiatum, SLM = Stratum Lacunosum Moleculare.
582 •= P < 0.05; ** = P < 0.01; ns = not significant.
583 Scale for A-B = 20 µm.
584
585 **REFERENCES**

586 Alexander, Georgia M, Logan Y Brown, Shannon Farris, Daniel Lustberg, Caroline Pantazis, Bernd Gloss,
587 Nicholas W Plummer, Patricia Jensen, and Serena M Dudek. 2018. "CA2 Neuronal Activity Controls
588 Hippocampal Low Gamma and Ripple Oscillations." ELife 7 (November): e38052.
589 https://doi.org/10.7554/eLife.38052.

590 Amchenkova, A A, L E Bakeeva, Y S Chentsov, V P Skulachev, and D B Zorov. 1988. "Coupling Membranes
591 as Energy-Transmitting Cables. I. Filamentous Mitochondria in Fibroblasts and Mitochondrial Clusters in
592 Cardiomyocytes." Journal of Cell Biology 107 (2): 481–95. https://doi.org/10.1083/jcb.107.2.481.

593 Asano, Shoh M., Ruixuan Gao, Asmamaw T. Wassie, Paul W. Tillberg, Fei Chen, and Edward S. Boyden.
594 2018. "Expansion Microscopy: Protocols for Imaging Proteins and RNA in Cells and Tissues." Current
595 Protocols in Cell Biology 80 (1). https://doi.org/10.1002/cpcb.56.

596 Ashrafi, Ghazaleh, Jaime de Juan-Sanz, Ryan J. Farrell, and Timothy A. Ryan. 2020. "Molecular Tuning of the
597 Axonal Mitochondrial Ca2+ Uniporter Ensures Metabolic Flexibility of Neurotransmission." Neuron 105 (4):
598 678-687.e5. https://doi.org/10.1016/j.neuron.2019.11.020.

599 Baughman, Joshua M., Fabiana Perocchi, Hany S. Girgis, Molly Plovanich, Casey A. Belcher-Timme, Yasemin
600 Sancak, X. Robert Bao, et al. 2011. "Integrative Genomics Identifies MCU as an Essential Component of the
601 Mitochondrial Calcium Uniporter." Nature 476 (7360): 341–45. https://doi.org/10.1038/nature10234.

602 Campbell, Logan A., Katy E. Pannoni, Niesha A. Savory, Dinesh Lal, and Shannon Farris. 2021. "Protein-
603 Retention Expansion Microscopy for Visualizing Subcellular Organelles in Fixed Brain Tissue." Journal of
604 Neuroscience Methods 361 (September): 109285. https://doi.org/10.1016/j.jneumeth.2021.109285.

605 Chang, D. T. W., A. S. Honick, and I. J. Reynolds. 2006. "Mitochondrial Trafficking to Synapses in Cultured
606 Primary Cortical Neurons." Journal of Neuroscience 26 (26): 7035–45.
607 https://doi.org/10.1523/JNEUROSCI.1012-06.2006.

608 Chevaleyre, Vivien, and Steven A. Siegelbaum. 2010. "Strong CA2 Pyramidal Neuron Synapses Define a
609 Powerful Disynaptic Cortico-Hippocampal Loop." Neuron 66 (4): 560–72.
610 https://doi.org/10.1016/j.neuron.2010.04.013.

611 De Stefani, Diego, Anna Raffaello, Enrico Teardo, Ildikò Szabò, and Rosario Rizzuto. 2011. "A Forty-Kilodalton
612 Protein of the Inner Membrane Is the Mitochondrial Calcium Uniporter." Nature 476 (7360): 336–40.
613 https://doi.org/10.1038/nature10230.

614 Devine, Michael J., and Josef T. Kittler. 2018. "Mitochondria at the Neuronal Presynapse in Health and
615 Disease." Nature Reviews Neuroscience 19 (2): 63–80. https://doi.org/10.1038/nrn.2017.170.

616 Divakaruni, Sai Sachin, Adam M. Van Dyke, Ramesh Chandra, Tara A. LeGates, Minerva Contreras, Poorna
617 A. Dharmasri, Henry N. Higgs, Mary Kay Lobo, Scott M. Thompson, and Thomas A. Blanpied. 2018. "Long-
618 Term Potentiation Requires a Rapid Burst of Dendritic Mitochondrial Fission during Induction." Neuron 100 (4):
619 860-875.e7. https://doi.org/10.1016/j.neuron.2018.09.025.

620 Drago, Ilaria, and Ronald L. Davis. 2016. “Inhibiting the Mitochondrial Calcium Uniporter during Development
621 Impairs Memory in Adult Drosophila.” Cell Reports 16 (10): 2763–76.
622 https://doi.org/10.1016/j.celrep.2016.08.017.

623 Duchen, M. R. 2000. “Mitochondria and Calcium: From Cell Signalling to Cell Death.” The Journal of
624 Physiology 529 Pt 1 (November): 57–68. https://doi.org/10.1111/j.1469-7793.2000.00057.x.

625 Dudek, Serena M., Georgia M. Alexander, and Shannon Farris. 2016. “Rediscovering Area CA2: Unique
626 Properties and Functions.” Nature Reviews. Neuroscience 17 (2): 89–102. https://doi.org/10.1038/nrn.2015.22.

627 Farris, Shannon, James M. Ward, Kelly E. Carstens, Mahsa Samadi, Yu Wang, and Serena M. Dudek. 2019.
628 “Hippocampal Subregions Express Distinct Dendritic Transcriptomes That Reveal Differences in Mitochondrial
629 Function in CA2.” Cell Reports 29 (2): 522-539.e6. https://doi.org/10.1016/j.celrep.2019.08.093.

630 Fecher, Caroline, Laura Trovò, Stephan A. Müller, Nicolas Snaidero, Jennifer Wettmarshausen, Sylvia Heink,
631 Oskar Ortiz, et al. 2019. “Cell-Type-Specific Profiling of Brain Mitochondria Reveals Functional and Molecular
632 Diversity.” Nature Neuroscience 22 (10): 1731–42. https://doi.org/10.1038/s41593-019-0479-z.

633 Granatiero, Veronica, Marco Pacifici, Anna Raffaello, Diego De Stefani, and Rosario Rizzuto. 2019.
634 “Overexpression of Mitochondrial Calcium Uniporter Causes Neuronal Death.” Oxidative Medicine and Cellular
635 Longevity 2019: 1681254. https://doi.org/10.1155/2019/1681254.

636 Han, Xiao-Jian, Yun-Fei Lu, Shun-Ai Li, Taku Kaitsuka, Yasufumi Sato, Kazuhito Tomizawa, Angus C. Nairn,
637 Kohji Takei, Hideki Matsui, and Masayuki Matsushita. 2008. “CaM Kinase Iα–Induced Phosphorylation of Drp1
638 Regulates Mitochondrial Morphology.” Journal of Cell Biology 182 (3): 573–85.
639 https://doi.org/10.1083/jcb.200802164.

640 Helton, Thomas D., Meilan Zhao, Shannon Farris, and Serena M. Dudek. 2019. “Diversity of Dendritic
641 Morphology and Entorhinal Cortex Synaptic Effectiveness in Mouse CA2 Pyramidal Neurons.” Hippocampus
642 29 (2): 78–92. https://doi.org/10.1002/hipo.23012.

643 Hitti, Frederick L., and Steven A. Siegelbaum. 2014. “The Hippocampal CA2 Region Is Essential for Social
644 Memory.” Nature 508 (7494): 88–92. https://doi.org/10.1038/nature13028.

645 Hutto, Rachel A., Celia M. Bisbach, Fatima Abbas, Daniel C. Brock, Whitney M. Cleghorn, Edward D. Parker,
646 Benjamin H. Bauer, et al. 2020. “Increasing Ca2+ in Photoreceptor Mitochondria Alters Metabolites,
647 Accelerates Photoresponse Recovery, and Reveals Adaptations to Mitochondrial Stress.” Cell Death &
648 Differentiation 27 (3): 1067–85. https://doi.org/10.1038/s41418-019-0398-2.

649 Kalyuzhny, A. E., J. Taylor, A. Ptak, P. Wood, D. Miller, H. Maple. Novel mitochondria marker for staining
650 formaldehyde fixed cells and tissue sections. Program No. P368.04. 2021 Neuroscience Meeting Planner.
651 Chicago, IL: Society for Neuroscience Global Connectome, 2021. Online.

652 Kedra, Joseph, Shen Lin, Almudena Pacheco, Gianluca Gallo, and George M. Smith. 2021. “Axotomy Induces
653 Drp1-Dependent Fragmentation of Axonal Mitochondria.” Frontiers in Molecular Neuroscience 14 (June):
654 668670. https://doi.org/10.3389/fnmol.2021.668670.

655 Kwong, Jennifer Q., Xiyuan Lu, Robert N. Correll, Jennifer A. Schwanekamp, Ronald J. Vagnozzi, Michelle A.
656 Sargent, Allen J. York, Jianyi Zhang, Donald M. Bers, and Jeffery D. Molkentin. 2015. “The Mitochondrial
657 Calcium Uniporter Selectively Matches Metabolic Output to Acute Contractile Stress in the Heart.” Cell Reports
658 12 (1): 15–22. https://doi.org/10.1016/j.celrep.2015.06.002.

Lee, Annie, Chandana Kondapalli, Daniel M. Virga, Tommy L. Lewis, So Yeon Koo, Archana Ashok, Georges Mairet-Coello, et al. 2019. “Aβ42 Oligomers Trigger Synaptic Loss through CAMKK2-AMPK-Dependent Effectors Coordinating Mitochondrial Fission and Mitophagy.” Preprint. Neuroscience. https://doi.org/10.1101/637199.

Lewis, Tommy L., Seok-Kyu Kwon, Annie Lee, Reuben Shaw, and Franck Polleux. 2018. “MFF-Dependent Mitochondrial Fission Regulates Presynaptic Release and Axon Branching by Limiting Axonal Mitochondria Size.” Nature Communications 9 (1): 5008. https://doi.org/10.1038/s41467-018-07416-2.

Li, Zheng, Ken-Ichi Okamoto, Yasunori Hayashi, and Morgan Sheng. 2004. “The Importance of Dendritic Mitochondria in the Morphogenesis and Plasticity of Spines and Synapses.” Cell 119 (6): 873–87. https://doi.org/10.1016/j.cell.2004.11.003.

Llorente-Folch, I., C. B. Rueda, B. Pardo, G. Szabadkai, M. R. Duchen, and J. Satrustegui. 2015. “The Regulation of Neuronal Mitochondrial Metabolism by Calcium: Regulation of Neuronal Mitochondrial Metabolism.” The Journal of Physiology 593 (16): 3447–62. https://doi.org/10.1113/JP270254.

Lopez-Rojas, Jeffrey, Christopher A. de Solis, Felix Leroy, Eric R. Kandel, and Steven A. Siegelbaum. 2021. “A Direct Lateral Entorhinal Cortex to Hippocampal CA2 Circuit Conveys Social Information Required for Social Memory.” Preprint. Neuroscience. https://doi.org/10.1101/2021.04.15.440048.

Luongo, Timothy S., Jonathan P. Lambert, Ancai Yuan, Xueqian Zhang, Polina Gross, Jianliang Song, Santhanam Shanmughapriya, et al. 2015. “The Mitochondrial Calcium Uniporter Matches Energetic Supply with Cardiac Workload during Stress and Modulates Permeability Transition.” Cell Reports 12 (1): 23–34. https://doi.org/10.1016/j.celrep.2015.06.017.

Madisen, Linda, Theresa A Zwingman, Susan M Sunkin, Seung Wook Oh, Hatim A Zariwala, Hong Gu, Lydia L Ng, et al. 2010. “A Robust and High-Throughput Cre Reporting and Characterization System for the Whole Mouse Brain.” Nature Neuroscience 13 (1): 133–40. https://doi.org/10.1038/nn.2467.

Mishra, Prashant, Valerio Carelli, Giovanni Manfredi, and David C. Chan. 2014. “Proteolytic Cleavage of Opa1 Stimulates Mitochondrial Inner Membrane Fusion and Couples Fusion to Oxidative Phosphorylation.” Cell Metabolism 19 (4): 630–41. https://doi.org/10.1016/j.cmet.2014.03.011.

Paillard, Melanie, György Csordás, Gergö Szanda, Tünde Golenár, Valentina Debattisti, Adam Bartok, Nadan Wang, et al. 2017. “Tissue-Specific Mitochondrial Decoding of Cytoplasmic Ca 2+ Signals Is Controlled by the Stoichiometry of MICU1/2 and MCU.” Cell Reports 18 (10): 2291–2300. https://doi.org/10.1016/j.celrep.2017.02.032.

Qiu, Jing, Yan-Wei Tan, Anna M. Hagenston, Marc-Andre Martel, Niclas Kneisel, Paul A. Skehel, David J. A. Wyllie, Hilmar Bading, and Giles E. Hardingham. 2013. “Mitochondrial Calcium Uniporter Mcu Controls Excitotoxicity and Is Transcriptionally Repressed by Neuroprotective Nuclear Calcium Signals.” Nature Communications 4 (1): 2034. https://doi.org/10.1038/ncomms3034.

Rangaraju, Vidhya, Marcel Lauterbach, and Erin M. Schuman. 2019. “Spatially Stable Mitochondrial Compartments Fuel Local Translation during Plasticity.” Cell 176 (1–2): 73-84.e15. https://doi.org/10.1016/j.cell.2018.12.013.

Schindelin, Johannes, Ignacio Arganda-Carreras, Erwin Frise, Verena Kaynig, Mark Longair, Tobias Pietzsch, Stephan Preibisch, et al. 2012. “Fiji: An Open-Source Platform for Biological-Image Analysis.” Nature Methods 9 (7): 676–82. https://doi.org/10.1038/nmeth.2019.

Simons, S. B., Y. Escobedo, R. Yasuda, and S. M. Dudek. 2009. “Regional Differences in Hippocampal Calcium Handling Provide a Cellular Mechanism for Limiting Plasticity.” Proceedings of the National Academy of Sciences 106 (33): 14080–84. https://doi.org/10.1073/pnas.0904775106.

Smith, Heather L, Jennifer N Bourne, Guan Cao, Michael A Chirillo, Linnaea E Ostroff, Deborah J Watson, and Kristen M Harris. 2016. “Mitochondrial Support of Persistent Presynaptic Vesicle Mobilization with Age-Dependent Synaptic Growth after LTP.” ELife 5 (December): e15275. https://doi.org/10.7554/eLife.15275.

Sprenger, Hans-Georg, and Thomas Langer. 2019. “The Good and the Bad of Mitochondrial Breakups.” Trends in Cell Biology 29 (11): 888–900. https://doi.org/10.1016/j.tcb.2019.08.003.

Srinivas, Kalyan V., Eric W. Buss, Qian Sun, Bina Santoro, Hiroto Takahashi, Daniel A. Nicholson, and Steven A. Siegelbaum. 2017. “The Dendrites of CA2 and CA1 Pyramidal Neurons Differentially Regulate Information Flow in the Cortico-Hippocampal Circuit.” The Journal of Neuroscience: The Official Journal of the Society for Neuroscience 37 (12): 3276–93. https://doi.org/10.1523/JNEUROSCI.2219-16.2017.

Stevenson, Erica L., and Heather K. Caldwell. 2014. “Lesions to the CA2 Region of the Hippocampus Impair Social Memory in Mice.” European Journal of Neuroscience 40 (9): 3294–3301. https://doi.org/10.1111/ejn.12689.

Steward, Oswald. 1976. “Topographic Organization of the Projections from the Entorhinal Area to the Hippocampal Formation of the Rat.” The Journal of Comparative Neurology 167 (3): 285–314. https://doi.org/10.1002/cne.901670303.

Stowers, R.Steven, Laura J. Megeath, Jolanta Górska-Andrzejak, Ian A. Meinertzhagen, and Thomas L. Schwarz. 2002. “Axonal Transport of Mitochondria to Synapses Depends on Milton, a Novel Drosophila Protein.” Neuron 36 (6): 1063–77. https://doi.org/10.1016/S0896-6273(02)01094-2.

Sun, Qian, Eric W. Buss, Yu-Qiu Jiang, Bina Santoro, David H. Brann, Daniel A. Nicholson, and Steven A. Siegelbaum. 2021. “Frequency-Dependent Synaptic Dynamics Differentially Tune CA1 and CA2 Pyramidal Neuron Responses to Cortical Input.” The Journal of Neuroscience 41 (39): 8103–10. https://doi.org/10.1523/JNEUROSCI.0451-20.2021.

Sun, Qian, Kalyan V Srinivas, Alaba Sotayo, and Steven A Siegelbaum. 2014. “Dendritic Na+ Spikes Enable Cortical Input to Drive Action Potential Output from Hippocampal CA2 Pyramidal Neurons.” ELife 3 (November): e04551. https://doi.org/10.7554/eLife.04551.

Tang, Yun-gui, and Robert S. Zucker. 1997. “Mitochondrial Involvement in Post-Tetanic Potentiation of Synaptic Transmission.” Neuron 18 (3): 483–91. https://doi.org/10.1016/S0896-6273(00)81248-9.

Vakifahmetoglu-Norberg, Helin, Amanda Tomie Ouchida, and Erik Norberg. 2017. “The Role of Mitochondria in Metabolism and Cell Death.” Biochemical and Biophysical Research Communications 482 (3): 426–31. https://doi.org/10.1016/j.bbrc.2016.11.088.

Wang, Xinnan, and Thomas L. Schwarz. 2009. “The Mechanism of Ca2+-Dependent Regulation of Kinesin-Mediated Mitochondrial Motility.” Cell 136 (1): 163–74. https://doi.org/10.1016/j.cell.2008.11.046.

Wescott, Andrew P., Joseph P. Y. Kao, W. Jonathan Lederer, and Liron Boyman. 2019. “Voltage-Energized Calcium-Sensitive ATP Production by Mitochondria.” Nature Metabolism 1 (10): 975–84. https://doi.org/10.1038/s42255-019-0126-8.

Zhao, Lantao, Shuhong Li, Shilei Wang, Ning Yu, and Jia Liu. 2015. “The Effect of Mitochondrial Calcium Uniporter on Mitochondrial Fission in Hippocampus Cells Ischemia/Reperfusion Injury.” Biochemical and Biophysical Research Communications 461 (3): 537–42. https://doi.org/10.1016/j.bbrc.2015.04.066.

Zhao, M., Y.-S. Choi, K. Obrietan, and S. M. Dudek. 2007. “Synaptic Plasticity (and the Lack Thereof) in Hippocampal CA2 Neurons.” Journal of Neuroscience 27 (44): 12025–32. https://doi.org/10.1523/JNEUROSCI.4094-07.2007.

Zheng, Xianchong, Mimi Chen, Xiaojing Meng, Xinwei Chu, Chunqing Cai, and Fei Zou. 2017. “Phosphorylation of Dynamin-Related Protein 1 at Ser616 Regulates Mitochondrial Fission and Is Involved in Mitochondrial Calcium Uniporter-Mediated Neutrophil Polarization and Chemotaxis.” Molecular Immunology 87 (July): 23–32. https://doi.org/10.1016/j.molimm.2017.03.019.